Journal of Materials Chemistry C

Real time quantification of mixed ion and electron transfer associated with the doping of poly(3-hexylthiophene)

Journal:	*Journal of Materials Chemistry C*
Manuscript ID	TC-ART-01-2022-000001.R1
Article Type:	Paper
Date Submitted by the Author:	01-Apr-2022
Complete List of Authors:	Thakur, Ratul; Texas A&M University Easley, Alexandra D; Texas A&M University Wang, Shaoyang; Texas A&M University Zhang, Yiren; Cornell University Ober, Christopher; Cornell University Lutkenhaus, Jodie; Texas A&M University

ARTICLE

Real time quantification of mixed ion and electron transfer associated with the doping of poly(3-hexylthiophene)

Received 00th January 20xx,
Accepted 00th January 20xx

DOI: 10.1039/x0xx00000x

Ratul M. Thakur, [a] Alexandra D. Easley, [b] Shaoyang Wang,[a] Yiren Zhang,[c] Christopher K. Ober,[c] Jodie L. Lutkenhaus.*[ab]

Conjugated polymers have promising applications in electronics and energy storage due to the polymer's tunable conductivity and redox activity. For example, the conductivity of poly(3-hexylthiophene) (P3HT) is heavily dependent upon the doping level and the dopant type. This feature becomes especially important when considering P3HT or similar conjugated polymers for devices that require switching between electronic states (conductive vs insulating). In this study, the mechanism of mixed ion-electron transfer studied using electrochemical quartz crystal microbalance with dissipation monitoring (EQCM-D) is discussed. During cyclic voltammetry and galvanostatic charge-discharge experiments, the mass change of a P3HT film is monitored in real time. Distinct mass transfer regions are quantified as a function of doping level and potential, which are then correlated to changes with *in situ* conductance and spectroelectrochemical response. To identify the time scale at which the doping reaction transitions from kinetic to diffusion control, electrochemical impedance spectroscopy is coupled with EQCM-D. This work gives valuable insight into the nature of mixed ion-electron transfer, including its time scale, as it relates to the electronic properties of P3HT.

Introduction

Conjugated polymers allow for free electron migration through a pathway of overlapping π-orbitals[1, 2] and have potential applications in organic electronic materials,[3, 4] organic field-effect transistors (OFETs),[5, 6] organic electrochemical transistors (OECTs),[7-9] energy storage,[10-12] and photovoltaics.[13, 14] Interestingly, conjugated polymers display mixed ion-electron transport behaviour in which both ion and electrons move in a concerted fashion during operation. Specifically, the electronic conductivity of a conjugated polymer is dependent on the doping level, dopant type, and the morphology of the conjugated polymer.[15, 16] Understanding the nature of the conjugated polymer's doping process is vital for designing and fabricating high-performance devices because it ultimately impacts the polymer's electronic properties.[3]

Doping may occur through chemical or electrochemical means. In the case of chemical doping, the conjugated polymer is mixed with or exposed to the chemical dopant which then undergoes a charge transfer reaction;[17-19] for example, the conductivity of poly(3-hexylthiophene) (P3HT) changes from 10^{-4} to 48 S cm^{-1} upon chemical doping with tetrafluoro-7,7,8,8-tetracyanoquinodimethane (F4TCNQ).[20] In the case of electrochemical doping, an applied bias is used to oxidize or reduce the polymer and counterions transport into the film for charge neutrality;[21, 22] for example, the conductivity of poly(3-hexylthiophene)-b-poly(ethylene oxide) (P3HT-PEO) increases from 10^{-8} to 10^{-2} S cm^{-1} when electrochemically doped with bis(trifluoromethane) sulfonimide ($TFSI^-$).[23] Electrochemical doping and de-doping of conjugated polymers is also the basis for energy storage, such as pseudocapacitors and batteries, for which proper selection of the electrolyte and dopant ion is an important factor.[24, 25] Whether the case be chemical or electrochemical doping, quantifying the relationships between doping level and conductivity remain challenging because many observations are performed *ex situ*.

In this work, we focus upon P3HT because it is a popularly studied conjugated polymer[26, 27] that bears conductivities as high as 570 S/cm for the dopant $FeCl_3$.[28] Many studies have evaluated the effect of P3HT's doping level on the electrochemical properties, conductance, and charge transfer resistance using *ex situ* characterization techniques such as four-point probe and electrochemical impedance spectroscopy (EIS). In one example, Lim *et al*.[20] examined the relationship among approximate dopant concentration, conductivity, and crystal structure for which F4TCNQ was the dopant. As the dopant concentration increased to 10 mol % (by P3HT repeat unit), the layer spacing increased, the π-π spacing decreased, and the conductivity increased from 10^{-4} S/cm to 48 S/cm. Thomas *et al*.[29] studied the morphology of P3HT as a function of carrier density using operando grazing incidence X-ray scattering, where a decrease in the π-π spacing was observed upon doping by

[a] *Artie McFerrin Department of Chemical Engineering, Texas A&M University, College Station, Texas 77840, USA*
[b] *Department of Materials Science and Engineering, Texas A&M University, College Station, Texas 77840, USA*
[c] *Materials Science and Engineering, Cornell University, Ithaca, New York, USA.*
Electronic Supplementary Information (ESI) available: [details of any supplementary information available should be included here]. See DOI: 10.1039/x0xx00000x

$TFSI^-$ up to a certain concentration. Yamamoto *et al*.[30] studied the generation of charge carriers (polarons and bipolarons) in a regio-regular P3HT upon doping with $FeCl_3$ vapor using UV-Vis/NIR absorption spectroscopy, but the precise doping level at that time was not reported. Gonçalves *et al*.[31] investigated the overoxidation of P3HT using EIS, where ClO_4^- was the dopant. Although these techniques provide valuable insights into doping, conductivity, and structure, many of these *ex-situ* techniques are carried out in dry conditions, which do not fully capture the true state of the system (*e.g.,* caused by solvent swelling). Therefore, *in situ* measurements are required to fully resolve the real-time nature of the doping process.

The doping mechanism of P3HT[32] and other conjugated polymers[33-36] has been explored *in situ* previously using EQCM (electrochemical quartz crystal microbalance), UV-Vis spectroelectrochemistry, and conductance.[37-40] In one example, Flagg *et al.*[40] examined the apparent mass change of P3HT due to swelling caused by incoming anions and solvent with four different aqueous potassium electrolytes using EQCM simultaneously operated during cyclic voltammetry or an applied potential step. They observed that large, polarized ions such as PF_6^- and $TFSI^-$ were accompanied by fewer water molecules (2 and 0.5 water molecules per anion, respectively) as compared to smaller anions Cl^- and ClO_4^- (10 water molecules per anion). They also investigated the anion-dependant doping process, where they observed that the onset of the increase in mobility of the electronic carriers occurs at 0.003 charge per thiophene unit for ClO_4^-. They also report that the mobility saturates around $\sim 3 \times 10^{-2}$ cm^2 V^{-1} s^{-1} at $\sim 4 \times 10^{20}$ holes cm^{-3}, irrespective of the anion used. Neusser *et al*.[41] examined the solid state conductivity of P3HT with both *in-situ* and *ex-situ* measurements with PF_6^- as the anion. They observed a plateau in conductivity at doping levels above 20 % and a maximum conductivity of 224 S/cm at a doping level of 40 % in which the doping level was calculated based on the amount of charge injected per P3HT monomer unit. This plateau region was attributed to the existence of overlapping polaron and bipolaron states, observed using UV-Vis spectroscopy. Zayat *et al.*[21] investigated the *in-situ* electronic and ionic conductivity changes in P3HT as a function of electrochemical doping using EIS. They observed a five-orders of magnitude increase in electronic conductivity and a two-orders of magnitude increase in ionic conductivity as the P3HT film was oxidized from 3V to 4V *vs.* Li/Li^+. Thelen *et al.*[42] examined the correlation of $TFSI^-$ ion concentration with electronic mobility, crystal structure, and mesoscale morphology using *in-situ* X-ray scattering and EIS. They observed an increase in lamellar stacking distance, a decrease in the π−π stacking distance, and an exponential increase in hole mobility attributed to the doping process.

Taken together, this past literature shows that with an application of applied bias P3HT is oxidized, accompanied by an increase in film mass due to incoming anions and solvent, leading to the conversion of uncharged (undoped) sites to charged sites (polarons and bipolarons).[30, 41, 43] At the same time, the insertion of anions into P3HT results in a reversible change in the crystal lattice, where the lamellar spacing expands to accommodate the anion and the π-π stacking distance decreases.[42, 44] This manifests in an exceptional increase in the conductivity caused by the enhanced inter-chain charge transfer through the π-stacks along with intra-chain charge transfer.[45] This current state-of-knowledge yields a piece-meal understanding of doping, conductivity, and structural changes during the doping/de-doping process because many of these aforementioned studies used different dopants, processing techniques, or solvents. A unified understanding of how electrochemical doping influences film swelling, how electrochemical doping quantitatively correlates to conductivity, and how solvent participates in the dopant ion's transport is lacking.

Here, we quantify the *in-situ* electrochemical doping of P3HT to better understand how doping, solvent uptake, and conductivity inter-relate. As it will be shown, swelling caused by mass changes attributed to the electrochemical doping process allows for the identification of critical regimes that correlate with doping and conductivity. Doping levels were quantified using EQCM-D during cyclic voltammetry (CV) and galvanostatic charge-discharge (GCD) cycling, resulting in the observation of distinct doping regimes that correlate to the emergence of polaronic and bipolaronic states, as observed using UV-Vis/NIR spectroscopy. The *in-situ* conductance of P3HT was correlated with specific doping levels to further support the distinct doping regimes recognized from EQCM-D. Finally, EIS coupled with QCM-D was used to distinguish the nature of frequency-dependent mass transport within the P3HT thin film. Together, these *in situ* observations give an unprecedented view of the dynamic nature of doping, conductivity, and solvent participation.

Materials and methods

Materials

Poly(3-hexylthiohene) used in this work was synthesized via nickel-catalyzed Grignard metathesis (GRIM) polymerization to obtain low PDI and high regioregularity. The monomer 2,5-dibromo-3-hexylthiophene was purchased from Ark Pharm. and was used without further purification. Anhydrous tetrahydrofuran (THF) was distilled from sodium/benzophenone mixture before use. All other chemicals and solvents were purchased from Sigma-Aldrich and VWR. The detailed procedures of GRIM polymerization have been previously reported by the Ober group.[46] In order to narrow the MW distribution of the homopolymer, crude P3HT was subjected to sequential Soxhlet extraction with methanol, hexane, and chloroform. The target polymer was recovered from chloroform fraction and dried in vacuum oven at 40 °C overnight. The molar mass was 8000 g/mol, the dispersity was 1.1, and the regio-regularity was >95%.

EQCM-D

Quartz-crystal microbalance with dissipation measurements were performed on gold-coated, planar AT-cut quartz crystals as a substrate in a Q-sense E1 module (Biolin scientific) combined with

electrochemical measurements using a potentiostat (Interface 1000, Gamry Instruments and Solartron 1260/1280). First, a clean bare sensor was baselined in air and then in 0.5 M lithium triflate ($LiCF_3SO_3$) propylene carbonate electrolyte solution. Sensors were cleaned using water and acetone before spin-coating them with 40 µL of a 10 mg mL^{-1} P3HT solution in chloroform. The coated sensors were vapor-annealed for approximately 12 h using THF and then vacuum-dried for 12 h at room temperature to remove residual solvent. The crystallinity of P3HT annealed in this manner was 36.9 % as determined from differential scanning calorimetry, using an ideal melting enthalpy of 33 J/g.[42]

To determine the thickness of the P3HT film, the coated sensor in air was compared to the blank sensor, and the Sauerbrey model was applied using Qtools software; a typical P3HT thickness was 215 nm. After the baseline was performed, the cell was filled with 0.5 M $LiCF_3SO_3$ in propylene carbonate electrolyte and was statically equilibrated for 20 min. For electrochemical testing, a platinum plate was used as the counter electrode, silver wire was used as the quasi-reference electrode (QRE), and the P3HT-coated sensor was used as the working electrode. All experiments were conducted at room temperature. The P3HT was conditioned by performing 20 cyclic voltammetry (CV) cycles at a scan rate of 10 mV/s. After conditioning, two CV cycles each at 1, 2, 5, 10, 25, and 50 mV/s were performed (**Figure S1**). This was followed by galvanostatic charge-discharge for three cycles each at 5C, 10C, and 20C. The C-rate was calculated based upon the mass coated on the sensor, where 1C is the current required to discharge the P3HT-coating completely in one hour (assuming a theoretical capacity of 161 mAh g^{-1}, for which every thiophene unit is charged). For EIS, the sample was conditioned as before and then subjected to EIS. The frequency was varied from 100 kHz to 0.1 Hz with an AC voltage of 10 mV at varies biases.

EQCM-D data modelling and analysis

The frequency and dissipation were monitored during CV, GCD, and EIS experiments. The mass change was quantified using the Sauerbrey model in Qtools software. Modelling was carried out using the third, fifth and seventh overtones with the goal of minimizing the χ^2 value. Specific fluid properties were also required for modelling and calculating the mass change. 0.5M lithium triflate in propylene carbonate was used as the electrolyte (viscosity of 0.0025 kg m^{-1} s^{-1} and density of 1200 kg m^{-3}). The density of the polymer was assumed to be same as of propylene carbonate.[47, 48] For analysis of the CVs, an "'equal area baseline" correction was used, which assumes that the amount of charge stored or released during each ½-cycle is equivalent. An iterative approach is used (**Figure S2**), in which a line dividing the CV into two halves is drawn and the charge stored and released is calculated. The slope of this line is iteratively changed until the charges of both halves are equal. Then, the charge versus time data is extracted for both oxidation and reduction halves using the final baseline. For GCD, the charge versus time data were obtained by simply integrating the applied current.

UV-Vis spectroscopy and spectroelectrochemistry

P3HT solution with a concentration of 2 mg/ml was drop-cast onto ITO-coated glass to obtain a P3HT film approximately 110 nm thick. The films were vapor-annealed as before. Before measurements, a baseline was obtained using blank ITO-coated glass immersed in electrolyte. The electrochemical cell consisted of P3HT-coated ITO-coated glass as the working electrode, silver wire as the QRE, platinum wire as the counter electrode, and 0.5 M of $LiCF_3SO_3$ in propylene carbonate as the electrolyte. The measurements were taken at increments of 0.1 V vs QRE starting from 0 V to 1 V. All spectroelectrochemical experiments were carried out using a Hitachi U-4100 UV-Vis-NIR spectrophotometer (341-F) and a Gamry Instrument Interface 1000 potentiostat. The change in substrate

In-situ conductance measurements

A home-built bipotentiostat setup was used to monitor the conductance of P3HT during electrochemical interrogation (*i.e.,* CV). The setup consisted of two separate poteniostats and interdigitated array electrodes (IDAs from BASi). The P3HT-coated IDA electrode served as the working electrode. A complete description is provided in **Scheme S1**.

Results

To assess the nature of mass transport in P3HT, we first performed EQCM-D simultaneously with cyclic voltammetry. **Figure 1** shows the response at scan rates of 1, 2, 5, 10, 25, 50 mV/s with respect to time. **Figure 1a, b,** and **c** show the input voltage, output current, and the charge passed (Q, calculated from the integrated current), respectively. **Figure 1d** and **e** show the frequency and dissipation for the third overtone, respectively, for which changes in frequency closely mirrored changes in Q. On the other hand, changes in dissipation were minor, indicating the rigidity of the film. Accordingly, the change in the P3HT electrode's mass, Δm, was obtained using the Sauerbrey model, **Figure 1f**. The general observation was that the electrode's mass increased during oxidation due to the ingress of triflate ions and solvent from the bulk electrolyte. During reduction, the electrode's mass decreased due to the egress of triflate ions and solvent. For each complete cycle, little-to-no mass accumulation was observed.

From these cyclic voltammetry results, trends in mass transport, electron transfer, and the doping level of P3HT were compared. **Figure 2a** plots Δm *vs* Q for a cyclic voltammogram taken at a scan rate of 10 mV/s, for which the slope represents the mass of the transporting species per mole of charge transferred (Δm/Q). A closer inspection of **Figure 2a** reveals three distinct linear regions (***FI***, ***FII***, and ***FIII***). Assuming only a triflate anion (no solvent) dopes an individual P3HT unit, a value of Δm/Q=1.55 μg/mC would result. Specific to the forward oxidation scan, positive deviations from this value would reflect the ingress of solvent along with the anion; negative deviations would reflect

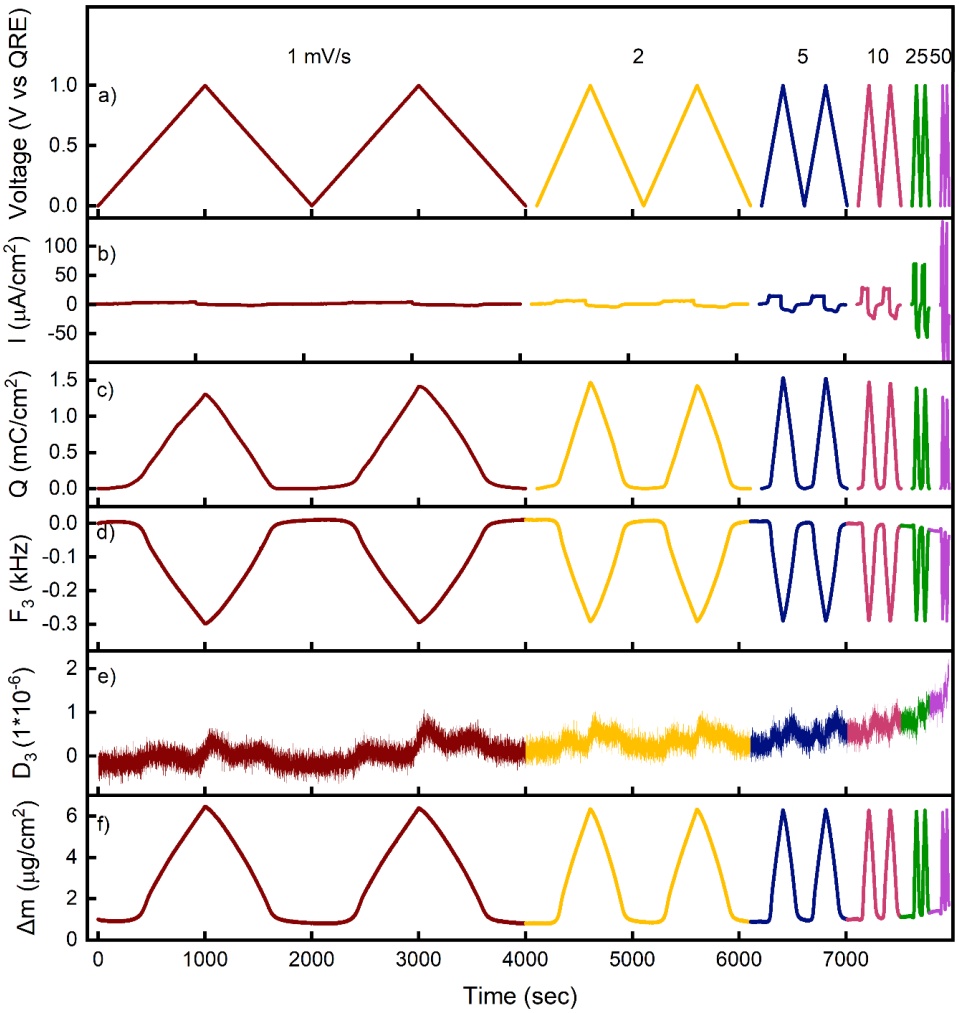

Figure 1. a) Voltage, b) current, c) charge transferred, d) third overtone frequency (F_3), e) third overtone dissipation (D_3), and f) mass change for the duration of the EQCM-D experiment and cyclic voltammetry over different scan rates. Here, and in other figures, P3HT was spin-coated onto a gold-coated sensor, annealed, and dried to form the working electrode. The counter electrode was a platinum plate, the quasi-reference electrode was a silver wire, and the electrolyte was 0.5M $LiCF_3SO_3$ in propylene carbonate. Prior to measurements, the P3HT electrode was conditioned for 20 cycles at 10 mV/s to promote penetration of electrolyte and equilibration of the film with the testing environment.

mixed transport of lithium cations and triflate anions, possibly with solvent; and, last, negative values would indicate solvent or cation expulsion. The reverse interpretation holds true for the reduction scan.

To further understand the role of the coupled mass-electron-solvent transport, these three transport regions are displayed in corresponding plots of Q *vs* t and Δm *vs* doping %, **Figure 2b, c**, respectively. To obtain **Figure 2c**, the doping percentage was calculated by dividing the moles of electron transferred by the moles of P3HT repeat units in the film, assuming only one electron transfers per repeat unit. Comparing across **Figures 2a-c** and those of other scan rates (see **Figure S3, S4** and **Table S1**), the three transport regions are generalized below for the forward oxidation scans (FI, FII, FIII).

FI: This region is characterized by a negative or near-zero Δm/Q value, depending on scan rate. This behaviour is assigned to minor solvent or lithium expulsion.[33] Also in region FI, very little charge was transferred because of the absence of any redox reaction. This region generally covers potentials of 0-0.35 V and doping levels of 0 to 0.3%.

FII: This region is marked by a Δm/Q value that is much higher than 1.55 μg/mC, which indicates the transport of solvent into the film along with the anion. This is accompanied by an increase in Q and an increase in conductivity (see below) as the redox reaction initiates. This region generally covers potentials of 0.35-0.6 V and doping levels of 0.3 to 2-3%.

FIII: This region possesses a Δm/Q value that is somewhat higher than the theoretical value for lithium triflate, indicating that the

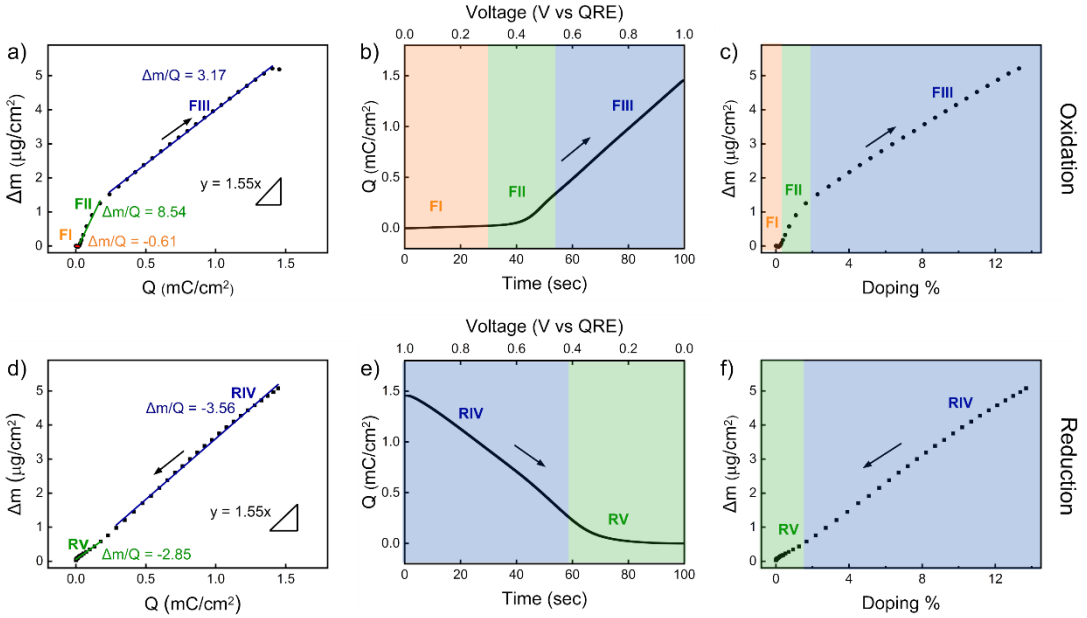

Figure 2. Coupled mass-electron transfer for P3HT during cyclic voltammetry. Mass change *vs* charge transferred for a) oxidation and d) reduction scans. Charge transferred with voltage and time for b) oxidation and e) reduction scans. Mass change *vs* doping percentage for c) oxidation and f) reduction scans. The scan rate was 10 mV/s.

incoming anions are still slightly solvated. This region generally covers potentials of 0.6-1.0 V and doping levels of 2-3 to 11-18%.

The reduction cycle is similarly classified into two regions based on the relative slopes of Δm vs Q, **Figure 2d. Figure 2e** shows the charge transferred with both voltage and time, whereas **Figure 2f** shows the change in mass with doping level. The two regions for the reverse scan are denoted as ***RIV*** and ***RV***. In region ***RIV***, both solvent and anion expulsion were observed. Most of the accumulated charge was released in the ***RIV*** region up to a doping level of 2.3%. In region ***RV***, a similar behaviour was observed, but with Δm/Q being slightly lower. This same analysis was carried out for scan rates varying from 1 to 50 mV/s, resulting in **Figure S5**, **S6** and **Table S1.** No strong trends with scan rate were observed, given the experimental error.

From the observed Δm/Q values in **Table S1**, the apparent molecular weight (M_w^{app}) of the transporting species was calculated using the Equation 1:

$$\frac{\Delta m}{\Delta Q} = \frac{M_w^{app}}{nF} \quad (1)$$

M_w^{app} represents the gain or loss of both the anion and solvent during the doping and de-doping process. Lithium cation transport was neglected for all regions, except for ***FI***. Using a mass balance approach, the number of solvent molecules accompanying each anion was estimated, **Table S2**. Region ***FII*** had the highest apparent molecular weight gain due to approximately 4-6 solvent molecules accompanying each transporting anion, depending on scan rate. In region ***FIII,*** the number of solvent molecules decreased to 1-2 molecules per transporting anion. In the reduction cycle, most of the solvent expulsion occurred in ***RIV*** with 1.5 to 2 solvent molecules per anion, whereas the transporting solvent decreased to 0.5 molecules per anion in ***RV***.

GCD cycling is a common electrochemical testing method applied to mimic practical battery or capacitor use.[49] Here, EQCM-D was combined with GCD to track gravimetric changes of a P3HT film subjected to constant current, **Figure 3**. The C-rates were restricted to 5, 10 and, 20 because lower C-rates resulted in self-discharging and significant charge hysteresis.[50, 51] C-rates greater than 20 led to very fast doping/de-doping, making it difficult to observe mass change within the resolution of the instrumentation.

Similar to the cyclic voltammetry analysis, mass transport, charge transfer and doping levels were correlated for the GCD experiments. **Figure 4a** plots Δm *vs* Q for GCD along with regions associated with the distinct Δm/Q slopes during oxidation for 10 C (0.046 mA/cm²). **Figure 4b** shows the change in charge transferred with voltage, whereas **Figure 4c** plots the change in mass with doping level. Among the two identified regions for oxidation, ***FI*** had a greater Δm/Q value as compared to ***FII,*** reflecting that incoming anions were more solvated in the early stages of oxidation. Specifically, Δm/Q for ***FII*** was comparable to the theoretical Δm/Q value for the triflate anion alone (no solvent). Notably, the doping level that separated the two regions was 3% - similar to the doping level (2-3%) separating regions ***FII*** and ***FIII*** from cyclic voltammetry. However, GCD results did not indicate any cation movement, as had been observed earlier for cyclic voltammetry (see ***FI***). For the reduction cycle, the mass change with charge transferred was uniform across the entire discharge cycle, manifesting in a constant Δm *vs* Q slope (***RIII***), as shown in

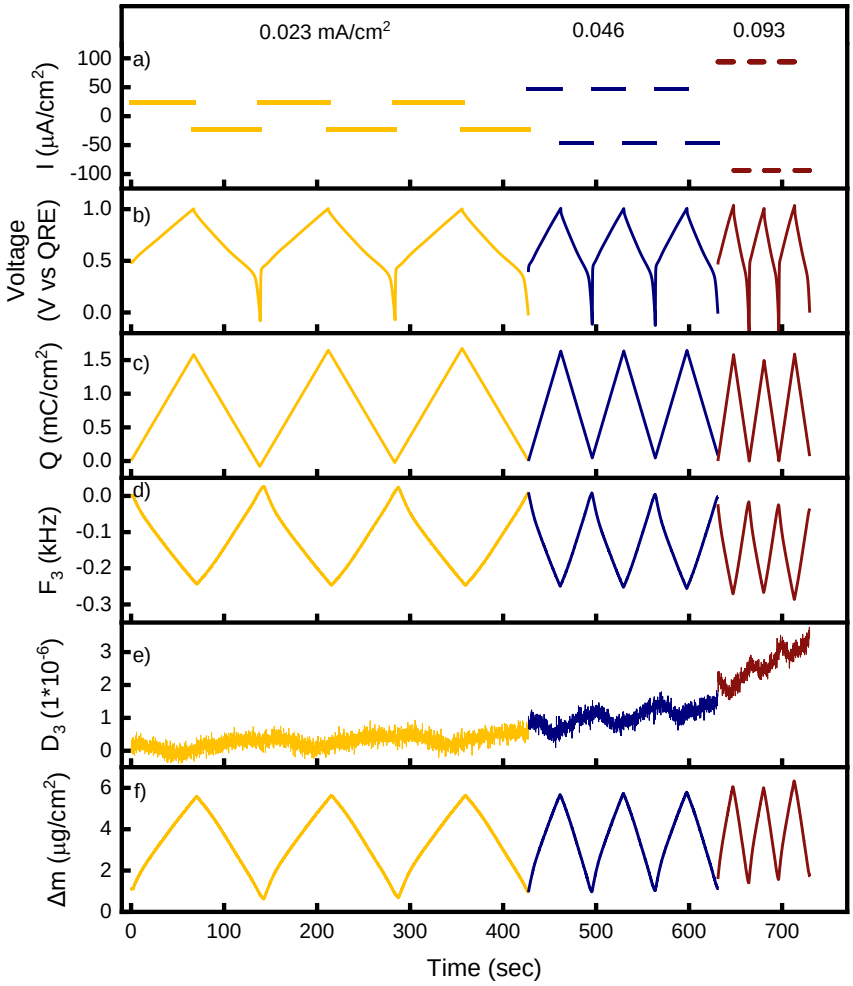

Figure 3. a) Current at 5 C, 10 C, and 20 C-rate (0.023, 0.046, and 0.093 mA/cm^2, respectively), b) voltage, c) charge transferred, d) third overtone frequency (F_3), e) third overtone dissipation (D_3), and f) mass change during the duration of the QCM-D experiment along with galvanostatic charge-discharge for different current densities.

Figure 4d. **Figure 4e** and **4f** show the charge transferred *vs* time and Δm *vs* doping %, respectively. Similar to the scan rate analysis, we performed for cyclic voltammetry, we also analysed the C-rate response for GCD cycling, resulting in **Figure S7, S8** and **Table S5**. M_w^{app} and the number of solvent molecules transported per anion are listed in **Table S6**. We generally observed an increase in Δm/Q and M_w^{app} values with increasing C-rate for ***FII*** and ***RIII*** regions, suggesting an increase in the accompanying solvent (1-2 solvent molecules per anion).

Given the preceding results, we now summarize and discuss the rate-dependency of the doping levels that demarcate the regions previously described, here-called the "transition doping percentage". We generally observed that, regardless of scan rate or C-rate, the transition doping percentages were relatively constant within an oxidation or reduction scan, **Figure 5**. **Figure 5a** shows Δm vs doping percentage for P3HT during oxidation at varying scan rates from cyclic voltammetry; the transition doping percentage for ***FI*** to ***FII*** was 0.3-0.4%, whereas the percentage for ***FII*** to ***FIII*** was 2-3%. As for reduction, **Figure 5b** shows transition doping percentages for ***RIV*** to ***RV*** of 1.5-2%. **Table S7** lists the average transition doping percentages for three different trials of CV at varying scan rates as displayed in **Figure S9, S10, S11** and **S12**. **Figure 5c** and **5d** show the Δm vs doping percentages for P3HT during galvanostatic charge-discharge at varying C-rates. The transition doping level for ***FI*** to ***FII*** in the oxidation cycle was 3-3.5%. **Table S8** lists the average transition doping percentage for three different trials of GCD with varying C-rate as shown in **Figure S13**.

The oxidation of P3HT by applying a potential bias results in the formation of charged species (polarons and bipolarons).[43] To understand the emergence of these species with respect to the doping regions, we performed *in situ* spectro-electrochemistry. **Figure 6a** shows differential absorbance spectra vs wavelength with increasing potential (0 to 1 V) for which the absorption spectrum at 0 V was taken as the reference. ITO glass was used as the substrate which has a work function of 4.9 eV;[52] however, gold, which has a work function of 5.3 eV,[53] was used as the substrate for the preceding EQCM-D experiments. Because of this, voltage shifts in the

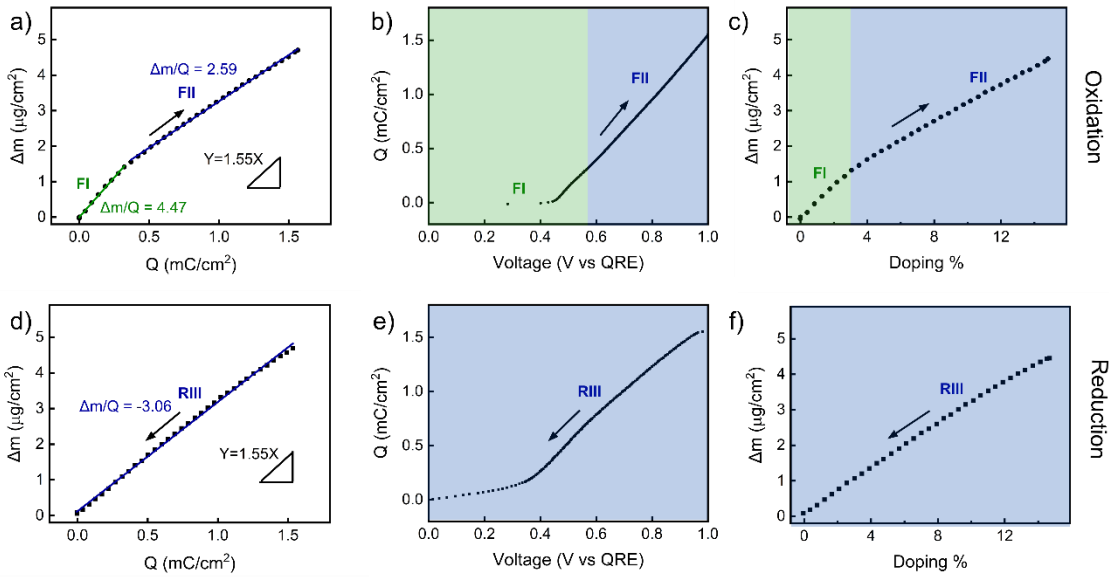

Figure 4. Coupled mass-electron transfer for P3HT during galvanostatic charge-discharge. Mass change vs charge transferred for a) oxidation and c) reduction. Charge transferred vs voltage for b) oxidation and e) reduction. Mass change vs doping percentage within the polymer film for c) oxidation and f) reduction at 10 C-rate.

electrochemical response of P3HT can occur, but this should not affect the overall doping mechanism for P3HT.

From the differential absorbance spectra, peaks for neutral (undoped) and charged P3HT species (polarons and bipolarons) were identified. Undoped P3HT shows a peak around 525 nm, assigned to the π-π* transition.[45] The wavelength of 805 nm is assigned to polarons and that of 1600 nm to bipolarons.[41, 43] **Figure 6b** shows the change in absorbance of the undoped, polaron, and bipolaron peaks with change in voltage. The coloured circles mark the voltages corresponding to the ***FI/FII*** and ***FII/FIII*** transitions identified from CV. Upon increasing the potential from 0 to 0.6 V, the absorption band for the undoped state remained fairly constant. Upon further increase in potential (from 0.6 to 1 V), the absorption band for the undoped state decreases; meanwhile the absorption bands for polaronic and bipolaronic species increase. Interestingly, the bipolaronic peak absorbance overtakes the polaronic one at the highest potentials. These results reflect the conversion of undoped P3HT species from a neutral state to charged states via doping.

To understand the implications on electronic conductivity, mass changes and conductance were measured using EQCM-D and a custom-built bipotentiostat setup, respectively, during cyclic voltammetry at a scan rate of 10 mV/s. **Figure 7a** shows Δm vs voltage for P3HT during oxidation, replotted from **Figure 1**. The inset of **Figure 7a** shows the magnified image for Δm vs voltage at the lower potential range (0 to 0.35V). The coloured circles reflect the potential at which the doping regions transition (as determined by changes in the slope of Δm vs Q in **Figure 2**). **Figure 7b** shows the change in current and conductance with voltage during oxidation at the same scan rate for P3HT cast onto an interdigitated microelectrode.

Using the real-time thickness of the swollen P3HT, the charge carrier concentration (Ne) and mobility (μ) during oxidation for a scan rate of 10 mV/s were plotted in **Figure 7c, Figure S14** and **ESI**. Using the real-time thickness to estimate these parameters is essential, but most other studies simply assume a constant thickness, introducing error. Also, **Figure 7d** shows the change in log (conductance) with log (doping fraction). In ***FI***, the conductance and mobility decrease, and Am remains fairly constant. In ***FII***, the conductance is at a minimum

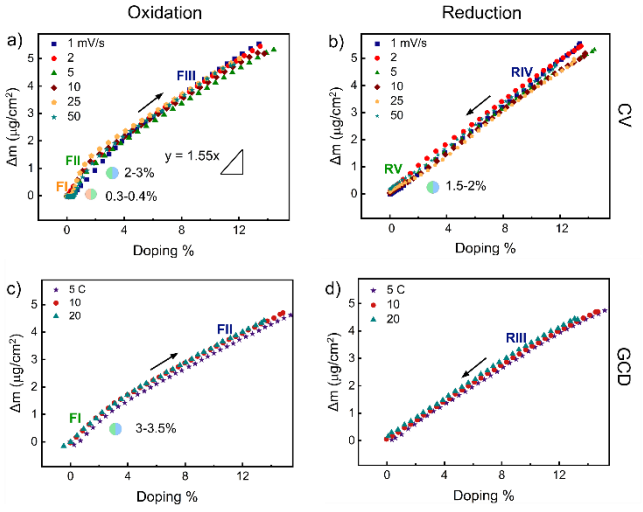

Figure 5. Mass change with doping percent at different scan rates for a) oxidation and b) reduction cyclic voltammetry scans. Mass change with doping percent at different C-rates for c) oxidation and d) reduction galvanostatic charge-discharge scans.

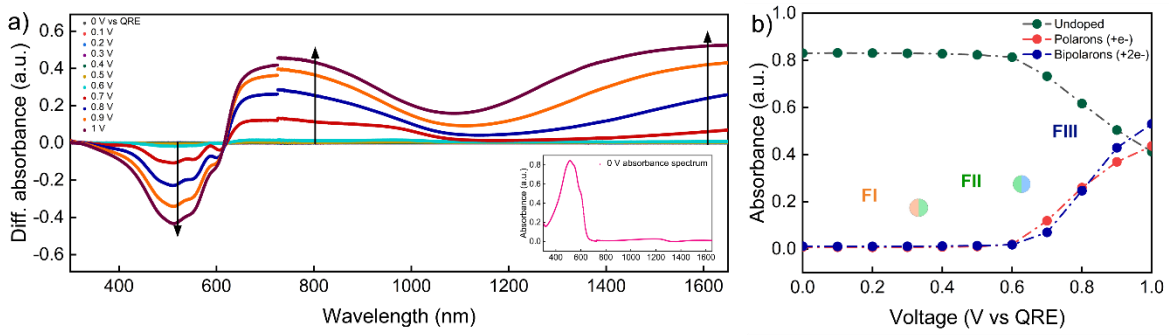

Figure 6. a) In situ UV–vis spectra of P3HT drop-cast on ITO-coated glass at held at selected potentials. The original spectrum of P3HT at 0 V (taken as reference) is inserted in the bottom right corner. b) Absorbance of P3HT at 525, 805, and 1600 nm, representing undoped, polaronic, and bipolaronic states, respectively, as a function of applied voltage. The P3HT film thickness was 115 ± 6 nm, and the background spectrum was ITO-coated glass immersed in electrolyte. The coloured circles show the voltage region at which the regions transition, identified from EQCMD, **Table S1**.

and then increases as voltage increases; Δm increases in this region due to incoming anions and solvent. Specifically, log(conductance) increasing linearly with log(Ne). The dependence of Ne with μ scales as $\mu \sim Ne^{0.83}$. In ***FIII***, this scaling increases in power as $\mu \sim Ne^{1.71}$ up to a carrier density of around 2.15×10^{20}, followed by a decrease. Taken together with the mass-response, this increase in mass and conductance are correlated to the doping of P3HT, as further confirmed by the emergence of the polaron and bipolaron peaks in the UV-Vis spectra, **Figure 6a**. **Figure S15a-d** shows a similar analysis for the reduction cycle. In ***RIV***, anions and solvent egress from the film, resulting in decreases in both mass and conductance. Overall, this oxidation-reduction cycle covered a two-orders of magnitude change in conductance of P3HT due to the doping process.

To understand the timescale of coupled ion-electron transfer, EIS with *in situ* EQCM-D was applied. To our knowledge, this is a first instance of coupling and analysing the two measurements in real-time. **Figure 8a** and **8b** show Nyquist and Bode plots, respectively, for P3HT under a sinusoidal bias of 10 mV at 0.9 V vs QRE, varying the frequencies from 100 kHz to 100 mHz. This potential was specifically selected to probe coupled transfer for P3HT in the intrinsically conductive state. **Figure 8c** shows the real-time mass change of P3HT during the EIS experiment. The experiment begins with the application of the highest frequency in the set, over which several periods of the sinusoidal bias are applied. Then, the next lower frequency is applied, and so on. The initial ~1600 ng/cm^2 increase in mass at very early times is attributed to the initial polarization of the electrode due to the application of the 0.9 V bias from the open circuit potential. At later times, the mass generally increased by only 1-1.2 ng sec^{-1} cm^{-2}, which we attribute to instrumental drift or gradual penetration of electrolyte into the P3HT film.

As the EIS frequency decreased, fluctuations in Δm associated with the applied sinusoidal bias were observed. Within a given EIS frequency, we analysed the amplitude of Δm, resulting in **Figure 8d**. At higher frequencies, the amplitude of Δm was relatively constant at about 5-10 ng/cm^2; this corresponds to the case of limited doping because of the short time scale. At lower frequencies, the amplitude of Δm increased; this corresponds to the case of the movement of ions with solvent during the redox reaction due to the longer timescale for diffusion. The coloured dot identifies the frequency (2.0 Hz) for which mass transport markedly increases, taken as the intersection of tangent lines drawn from the high and low frequency regions. Interestingly, this critical frequency value corresponds to the same frequency region at which the Nyquist plot shows a shift from reaction-controlled to diffusion-controlled behaviour. This analysis was carried out for other potentials (0.3-0.8 V) shown in **Figure S16, S17, S18 and S19**, for which the onset frequency decreased from 12.0 to 2.0 Hz with increasing bias, **Table S9**. Also, the diffusion coefficient for the $CF_3SO_3^-$ ion for higher voltages (0.7 V to 0.9 V) was calculated from the Warburg tail in the low-frequency region. The diffusion coefficient decreased from 2.7×10^{-15} cm^2/sec at 0.9 V to 3.7×10^{-17} cm^2/sec at 0.7 V. Taken, together these results indicate that diffusion and reaction proceed faster when P3HT is conductive.

Discussion

To connect the results of the three different *in-situ* measurements (EQCM-D, conductance, and UV-Vis spectroscopy) we revisit each doping region in the context of the cyclic voltammetry experiment for only oxidation.

FI, 0 V to 0.3-0.4 V vs QRE, 0% to 0.3-0.4% doped: At the early stages of oxidation, there is very low electrochemical activity, and the Δm/Q values are slightly negative or near-zero, characteristic of both minor solvent and/or lithium expulsion from the film. The polymer is mostly undoped, characterized by the relatively constant UV-Vis absorbance response, **Figure 6**. Conductance remains constant and low at ~$10^{-0.5}$ S until the late stages of ***FI*** in which the conductance abruptly drops to ~$10^{-1.2}$ S just as the change in mass becomes more positive (inset of **Figure 7a**). Meanwhile, mobility decreases with increasing charge carrier concentration, **Figure 7c**. Arkhipov *et al*. explained that a decrease in mobility with increasing charge carrier concentration at low doping levels is because of deep coulomb trap states.[54] This

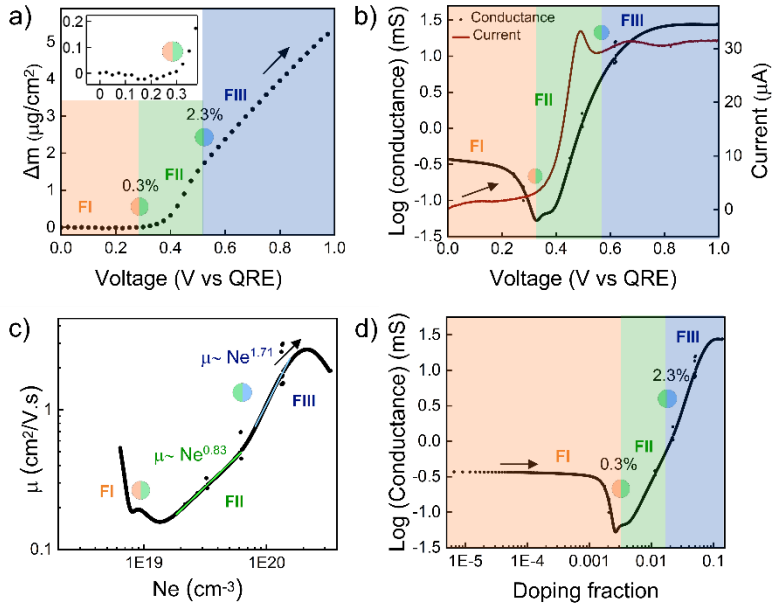

Figure 7. Real-time mass change, conductance, and mobility of P3HT undergoing cyclic voltammetry (oxidation sweep) at 10 mV/s. a) Mass change with voltage during oxidation; b) Corresponding conductance and current with voltage; c) Mobility with charge carrier concentration; and d) Log (conductance) with log (doping fraction). The coloured circles separate the different doping regions, as originally described in **Figure 2a** and **Table 1** from EQCM-D. The values assigned to the circles represent the transition doping percentage, as identified in **Figure 2c** and **Table S7**.

region may be referred to as the "***insulating region***", and its behaviour continues until a doping percentage of 0.3-0.4%. Elsewhere, cation expulsion has been reported elsewhere for the conjugated polymer poly (3-[2-(2-methoxyethoxy) ethoxy]methyl thiophene-2,5-diyl) (P3MEEMT), where the cation (K^+) was expelled from the film upon application of the initial oxidation bias.[34]

FII, 0.3-0.4 V to 0.55-0.6 V vs QRE, 0.3-0.4 to 2-3% doped: Proceeding further with oxidation, this region has relatively large Δm/Q values (**Table 1**) due to the injection of solvated anions. In the UV-Vis spectra, there is a slight increase in the absorbance band for the polaron and bipolaron peaks and a slight decrease in the undoped P3HT peak shown in **Figure 6b.** This reflects the initial conversion of P3HT units from a neutral state to a charged state upon applying an oxidizing potential. At the same time, there is a large increase in conductance due to the injection of the dopant anions, **Figure 7a, b. Figure 7d** shows a linear increase in log(conductance) with log(doping fraction), reflecting the exponential increase in conductance in this region. Also, the mobility increases with increasing charge carrier concentration ($\mu \sim Ne^{0.83}$). The formation of charged species (polarons and bipolarons) with increasing potential reduces the charge transfer resistance as shown from EIS **Table S7**. The **FII** region encompasses the switching of P3HT from its insulating to conducting states, up to a doping percentage of 2-3 %. **FII** may be referred to as the "***transitional region***".

FIII, 0.55-0.6 V to 1 V vs QRE, 2-3 % to 11-16% doped: At the final stages of oxidation, the Δm/Q values indicate the injection of solvated anions, but less solvent is transferred in comparison to ***FII*** (**Table 1**). There is a substantial increase in the polaron and bipolaron UV absorbance bands and a decrease in the undoped P3HT peak shown in **Figure 6b,** indicating the significant generation of charged species. At the same time, the mobility exponentially increases with increasing charge carrier concentration ($\mu \sim Ne^{1.71}$) resulting in an increase in the conductance of the P3HT film. The conductance reaches a maximum value and plateaus with voltage and doping fraction, as shown in **Figure 7b** and **Figure 7d** respectively. This region may arise from the formation of π- π stacking, facilitating interchain charge transfer along with intra chain charge transfer,[55, 56] and can be referred to as the "***conductive region***". This region also indicates that a critical charge carrier concentration ($Ne \sim 2.15 \times 10^{21}$) was attend, above which the charge carrier mobility decreases with an increase in carrier concentration (see **Figure 7c**). This decrease in mobility shows that carrier transport is governed by ionized impurity scattering at high doping levels.[57, 58] We speculate that the plateauing of the conductance with doping may be caused due to a combination of decreasing mobility and increasing charge carrier concentration. Higher levels of doping (or voltage) could not be achieved experimentally because P3HT exhibited instability (characterized by an upturn in current).

In a prior report, a similar analysis was carried out for PEDOT using EQCM for which three Δm/Q regions in the oxidation cycle and two regions in reduction cycle based were observed.[33] However, the exact doping levels for each region were not distinguished nor were they correlated to conductivity or spectrophotometric changes.

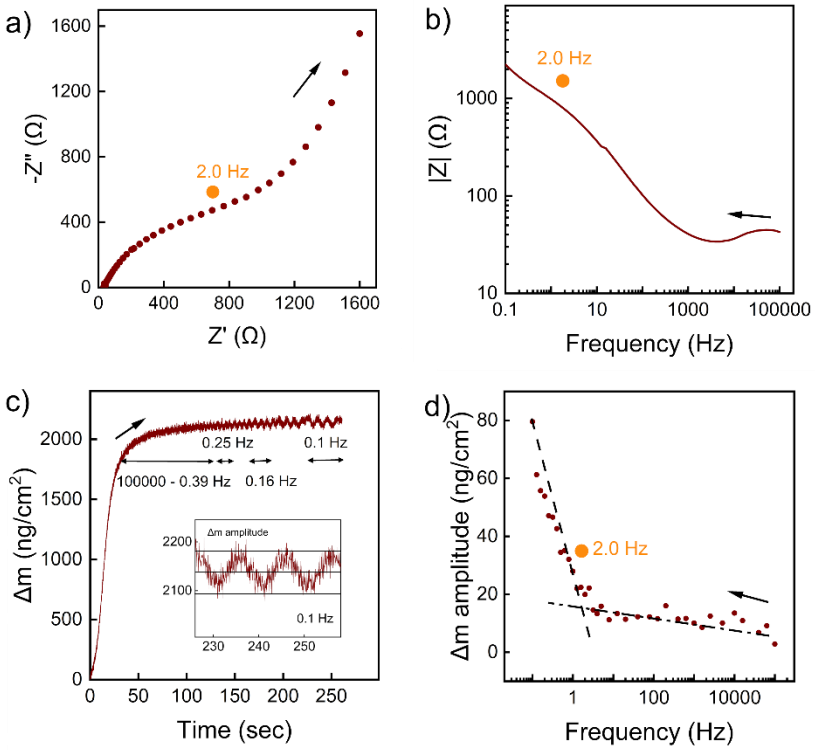

Figure 8. a) Nyquist and b) Bode plots, along with the simultaneous c) mass response of P3HT at 0.9 V vs QRE in the same configuration as Fig. 2. d) Amplitude of the mass change *vs* EIS frequency. The dot denotes the transition frequency for reaction- to diffusion-limited behavior. The arrow denotes the progression of time in the experiment itself.

Elsewhere, *in-situ* conductance and UV-Vis/NIR spectroelectrochemical measurements were carried out for PEDOT and PEDOT:PSS polymer films, where a sigmoidal conductance profile was obtained as voltage changed.[59] Upon increasing the potential bias, neutral PEDOT molecules oxidized to polarons and bipolarons species responsible for the high conductance plateau. The generation of charged species upon increasing the potential bias was also reported for P3HT during *in situ* UV-Vis/near-IR spectroelectrochemical measurements.[41, 43] Jiang *et al.* reports a similar trend for the change in conductivity with respect to doping level for P3HT.[60] Taken together, many studies have examined pieces of the conductivity-doping-mass transport problem for conjugated polymers, but none have considered it wholistically in the manner shown here.

One aspect that this study has not considered is the possibility of crystallographic changes during the electrochemical doping of P3HT. Previously, Thelen *et al.* performed XRD of P3HTs bearing different doping levels.[42] No change in width or peak area was observed regardless of the doping level, and the crystallinity (62%) remained constant. This indicates that incoming dopants do not affect the overall crystallinity of P3HT, but dopants do add to strain in the crystal lattice. The authors discussed that this strain contributes to a reduction of the π- π stacking distance, leading to an increase in hole mobility. Similar to P3HT, the *in-situ* change of crystal lattice was examined for PEDOT:PSS during doping and de-doping.[61] A reversible change in lamella *d*-spacing and π- π stacking distance was observed with potential. In the context of the work discussed here, changes in P3HT crystallinity due to electrochemical doping are assumed to be minor, but changes in crystal lattice structure may be influential. Giridharagopal *et al.*[62] examined local variation of ion transport in P3HT swollen with electrolyte using in situ electrochemical strain microscopy and observed preferential swelling in the amorphous regions. It is quite possible herein that swelling occurs in a similar fashion; more specifically, we observed thickness changes as much as 23% during cyclic voltammetry, **Figure S14**.

Conclusions

This work quantifies the real-time effects of mass transfer and electrochemical doping on the electronic properties of P3HT. Three doping regions were identified based on the nature of the mass transfer (by examination of Δm/Q) by combining cyclic voltammetry or galvanostatic cycling simultaneously operated with QCM-D. These measurements also allowed for the number of propylene carbonate molecules accompanying the triflate ion during doping to be quantified. In the "*conducting region*" for cyclic voltammetry, around 1-2 solvent molecules were transferred, and in the "*transitional region*", around 4-9 solvent molecules accompanied the triflate ion. For the case of galvanostatic cycling at the higher scan rates in

oxidation (>25 mV/s), more solvent is transferred due to the inability of the anion to fully shed its solvation shell. This study also recognized the formation of polarons and bipolarons in the "*transitional and conducting regions*", as confirmed using *in-situ* UV-Vis measurements. *In-situ* conductance measurements monitored the change in conductance across the three doping regions and revealed a strong correlation to the identified doping regions. Generally, the vast majority of ion transport can be assigned to the anion, for which anions egressing (de-doping) from the P3HT resulted in a decrease in conductance, whereas incoming anions (doping) increased the conductance by two orders of magnitude. The relationship between the change in mobility and charge carrier concentration was calculated using real-time data, including swollen thickness. For the "*transitional region*", μ is proportional to $Ne^{0.83}$ whereas μ is proportional to $Ne^{1.71}$ in the "*conducting region"*. The shift from an insulating state to a conducting state was confirmed using EIS, in which the charge transfer resistance decreased with increasing potential. EIS coupled with EQCM-D quantified the onset frequency responsible for a transition from reaction- to diffusion-limited behaviour (~1- 12Hz).

Future work should examine the structural or crystallographic evolution of this conjugated polymer during doping and de-doping to fully explain the distinctions among these doping regions. Additionally, various anions and cations of varying size and polarity should be investigated, as we expect those to strongly influence the nature of electrochemical doping in P3HT. Taken together, the analysis presented here provides a pathway to correlating mass transport with conductance at various time scales during real-time interrogation.

Conflicts of interest

There are no conflicts to declare.

Acknowledgements

This work was primarily supported by the Welch Foundation by grant A-2070-20210327 (Lutkenhaus). Synthesis work (Ober) was supported by grant DE-SC0014336 funded by the US Department of Energy, Office of Science.

Notes and references

[a.] The moles of solvent incoming were not calculated for FI due to presence of small negative slope.

1. T. Aoki, T. Kaneko and M. Teraguchi, *Polymer*, 2006, **47**, 4867-4892.
2. J. W. Onorato and C. K. Luscombe, *Molecular Systems Design & Engineering*, 2019, **4**, 310-324.
3. J. Chung, A. Khot, B. M. Savoie and B. W. Boudouris, *ACS Macro Letters*, 2020, **9**, 646-655.
4. R. M. Pankow and B. C. Thompson, *Polymer*, 2020, **207**, 122874.
5. S. Liu, W. M. Wang, A. L. Briseno, S. C. B. Mannsfeld and Z. Bao, *Advanced Materials*, 2009, **21**, 1217-1232.
6. S. Allard, M. Forster, B. Souharce, H. Thiem and U. Scherf, *Angew Chem Int Ed Engl*, 2008, **47**, 4070-4098.
7. J. Nightingale, C. Pitsalidis, A.-M. Pappa, E. Tan, K. Stewart, R. M. Owens and J.-S. Kim, *Journal of Materials Chemistry C*, 2020, **8**, 8846-8855.
8. J. T. Friedlein, M. J. Donahue, S. E. Shaheen, G. G. Malliaras and R. R. McLeod, *Advanced Materials*, 2016, **28**, 8398-8404.
9. E. Tan, A.-M. Pappa, C. Pitsalidis, J. Nightingale, S. Wood, F. A. Castro, R. M. Owens and J.-S. Kim, *Biotechnology and Bioengineering*, 2020, **117**, 291-299.
10. J. Xie, P. Gu and Q. Zhang, *ACS Energy Letters*, 2017, **2**, 1985-1996.
11. J. F. Mike and J. L. Lutkenhaus, *Journal of Polymer Science Part B: Polymer Physics*, 2013, **51**, 468-480.
12. C. K. Song, B. J. Eckstein, T. L. Tam, L. Trahey and T. J. Marks, *ACS Appl Mater Interfaces*, 2014, **6**, 19347-19354.
13. A. Facchetti, *Chemistry of Materials*, 2011, **23**, 733-758.
14. D. E. Motaung, G. F. Malgas, C. J. Arendse, S. E. Mavundla, C. J. Oliphant and D. Knoesen, *Solar Energy Materials and Solar Cells*, 2009, **93**, 1674-1680.
15. Z. Liang, Y. Zhang, M. Souri, X. Luo, Alex M. Boehm, R. Li, Y. Zhang, T. Wang, D.-Y. Kim, J. Mei, S. R. Marder and K. R. Graham, *Journal of Materials Chemistry A*, 2018, **6**, 16495-16505.
16. L.-S. Hornberger, D. Neusser, C. Malacrida, L. G. Kaake and S. Ludwigs, *Applied Physics Letters*, 2021, **119**, 163301.
17. S. E. Yoon, J. Park, J. E. Kwon, S. Y. Lee, J. M. Han, C. Y. Go, S. Choi, K. C. Kim, H. Seo, J. H. Kim and B.-G. Kim, *Advanced Materials*, 2020, **32**, 2005129.
18. D. T. Scholes, P. Y. Yee, G. R. McKeown, S. Li, H. Kang, J. R. Lindemuth, X. Xia, S. C. King, D. S. Seferos, S. H. Tolbert and B. J. Schwartz, *Chemistry of Materials*, 2019, **31**, 73-82.
19. W. Zhao, J. Ding, Y. Zou, C.-a. Di and D. Zhu, *Chemical Society Reviews*, 2020, **49**, 7210-7228.
20. E. Lim, K. A. Peterson, G. M. Su and M. L. Chabinyc, *Chemistry of Materials*, 2018, **30**, 998-1010.
21. B. Zayat, P. Das, B. C. Thompson and S. R. Narayan, *The Journal of Physical Chemistry C*, 2021, **125**, 7533-7541.
22. P. Shiri, D. Neusser, C. Malacrida, S. Ludwigs and L. G. Kaake, *The Journal of Physical Chemistry C*, 2021, **125**, 536-545.
23. S. N. Patel, A. E. Javier and N. P. Balsara, *ACS Nano*, 2013, **7**, 6056-6068.
24. Z. Yu, H. Wang, X. Kong, W. Huang, Y. Tsao, D. G. Mackanic, K. Wang, X. Wang, W. Huang, S. Choudhury, Y. Zheng, C. V. Amanchukwu, S. T. Hung, Y. Ma, E. G. Lomeli, J. Qin, Y. Cui and Z. Bao, *Nature Energy*, 2020, **5**, 526-533.
25. Q. Li, J. Chen, L. Fan, X. Kong and Y. Lu, *Green Energy & Environment*, 2016, **1**, 18-42.
26. A. Marrocchi, D. Lanari, A. Facchetti and L. Vaccaro, *Energy & Environmental Science*, 2012, **5**, 8457-8474.
27. P. Pingel and D. Neher, *Physical Review B*, 2013, **87**, 115209.
28. V. Vijayakumar, Y. Zhong, V. Untilova, M. Bahri, L. Herrmann, L. Biniek, N. Leclerc and M. Brinkmann, *Advanced Energy Materials*, 2019, **9**, 1900266.
29. E. M. Thomas, M. A. Brady, H. Nakayama, B. C. Popere, R. A. Segalman and M. L. Chabinyc, *Advanced Functional Materials*, 2018, **28**, 1803687.

30. J. Yamamoto and Y. Furukawa, *J Phys Chem B*, 2015, **119**, 4788-4794.
31. R. Gonçalves, *International Journal of Electrochemical Science*, 2017, DOI: 10.20964/2017.03.44, 1983-1991.
32. Y. Son, H. J. Park, J. S. Choi and Y. Lee, *Molecular Crystals and Liquid Crystals Science and Technology. Section A. Molecular Crystals and Liquid Crystals*, 2006, **349**, 343-346.
33. L. Zhang and T. L. Andrew, *Advanced Materials Interfaces*, 2017, **4**.
34. L. Q. Flagg, C. G. Bischak, R. J. Quezada, J. W. Onorato, C. K. Luscombe and D. S. Ginger, *ACS Materials Letters*, 2020, **2**, 254-260.
35. V. Syritski, A. Öpik and O. Forsén, *Electrochimica Acta*, 2003, **48**, 1409-1417.
36. C. G. Bischak, L. Q. Flagg, K. Yan, T. Rehman, D. W. Davies, R. J. Quezada, J. W. Onorato, C. K. Luscombe, Y. Diao, C.-Z. Li and D. S. Ginger, *Journal of the American Chemical Society*, 2020, **142**, 7434-7442.
37. C. Janáky, G. Cseh, P. S. Tóth and C. Visy, *Journal of Solid State Electrochemistry*, 2010, **14**, 1967-1973.
38. P. S. Tóth, G. F. Samu, B. Endrődi and C. Visy, *Electrochimica Acta*, 2013, **110**, 446-451.
39. F. Huerta, C. Quijada, F. Montilla and E. Morallón, *Journal of Electroanalytical Chemistry*, 2021, **897**, 115593.
40. L. Q. Flagg, R. Giridharagopal, J. Guo and D. S. Ginger, *Chemistry of Materials*, 2018, **30**, 5380-5389.
41. D. Neusser, C. Malacrida, M. Kern, Y. M. Gross, J. van Slageren and S. Ludwigs, *Chemistry of Materials*, 2020, **32**, 6003-6013.
42. J. L. Thelen, S.-L. Wu, A. E. Javier, V. Srinivasan, N. P. Balsara and S. N. Patel, *ACS Macro Letters*, 2015, **4**, 1386-1391.
43. C. Enengl, S. Enengl, S. Pluczyk, M. Havlicek, M. Lapkowski, H. Neugebauer and E. Ehrenfreund, *Chemphyschem*, 2016, **17**, 3836-3844.
44. J. K. Harris, B. Neelamraju and E. L. Ratcliff, *Chemistry of Materials*, 2019, **31**, 6870-6879.
45. M. Skompska and A. Szkurłat, *Electrochimica Acta*, 2001, **46**, 4007-4015.
46. Y. Zhang, A. M. Park, S. R. McMillan, N. J. Harmon, M. E. Flatté, G. D. Fuchs and C. K. Ober, *Chemistry of Materials*, 2018, **30**, 4799-4807.
47. S. Wang, F. Li, A. D. Easley and J. L. Lutkenhaus, *Nat Mater*, 2019, **18**, 69-75.
48. S. Wang, A. D. Easley, R. M. Thakur, T. Ma, J. Yun, Y. Zhang, C. K. Ober and J. L. Lutkenhaus, *Chemical Science*, 2020, **11**, 9962-9970.
49. A. Tomaszewska, Z. Chu, X. Feng, S. O'Kane, X. Liu, J. Chen, C. Ji, E. Endler, R. Li, L. Liu, Y. Li, S. Zheng, S. Vetterlein, M. Gao, J. Du, M. Parkes, M. Ouyang, M. Marinescu, G. Offer and B. Wu, *eTransportation*, 2019, **1**.
50. G. Milczarek and O. Inganäs, *Science*, 2012, **335**, 1468.
51. W. Viola, C. Jin and T. L. Andrew, *Synthetic Metals*, 2020, **268**, 116483.
52. Y. Yokokura, T. Dogase, T. Shinbo, Y. Nakayashiki, Y. Takagi, K. Ueda, K. Sarangerel, B. Delgertsetseg, C. Ganzorig and M. Sakomura, *AIP Advances*, 2017, **7**, 085321.
53. W. M. H. Sachtler, G. J. H. Dorgelo and A. A. Holscher, *Surface Science*, 1966, **5**, 221-229.
54. V. I. Arkhipov, E. V. Emelianova, P. Heremans and H. Bässler, *Physical Review B*, 2005, **72**, 235202.
55. G. Salinas and B. A. Frontana-Uribe, *ChemElectroChem*, 2019, **6**, 4105-4117.
56. C. Malacrida, Y. Lu, K. Dirnberger, S. Gámez-Valenzuela, M. C. Ruiz Delgado and S. Ludwigs, *Journal of Materials Chemistry C*, 2020, **8**, 15393-15405.
57. M. Heydari Gharahcheshmeh and K. K. Gleason, *Materials Today Advances*, 2020, **8**, 100086.
58. S. Lee, D. C. Paine and K. K. Gleason, *Advanced Functional Materials*, 2014, **24**, 7187-7196.
59. M. Wieland, C. Malacrida, Q. Yu, C. Schlewitz, L. Scapinello, A. Penoni and S. Ludwigs, *Flexible and Printed Electronics*, 2020, **5**, 014016.
60. X. Jiang, Y. Harima, K. Yamashita, Y. Tada, J. Ohshita and A. Kunai, *Chemical Physics Letters*, 2002, **364**, 616-620.
61. B. D. Paulsen, R. Wu, C. J. Takacs, H.-G. Steinrück, J. Strzalka, Q. Zhang, M. F. Toney and J. Rivnay, *Advanced Materials*, 2020, **32**, 2003404.
62. R. Giridharagopal, L. Q. Flagg, J. S. Harrison, M. E. Ziffer, J. Onorato, C. K. Luscombe and D. S. Ginger, *Nature Materials*, 2017, **16**, 737-742.